Schnurri-3 inhibition suppresses bone and joint damage in models of rheumatoid arthritis

Zheni Stavre[a,1] [ID], Jung-Min Kim[a,1] [ID], Yeon-Suk Yang[a], Kerstin Nündel[a] [ID], Sachin Chaugule[a] [ID], Tadatoshi Sato[a,b,c,d], Kwang Hwan Park[e] [ID], Guangping Gao[b,c,f,g] [ID], Ellen M. Gravallese[h,2] [ID], and Jae-Hyuck Shim[a,b,c,2] [ID]

Rheumatoid arthritis (RA) is a chronic inflammatory disease that leads to systemic and articular bone loss by activating bone resorption and suppressing bone formation. Despite current therapeutic agents, inflammation-induced bone loss in RA continues to be a significant clinical problem due to joint deformity and lack of articular and systemic bone repair. Here, we identify the suppressor of bone formation, Schnurri-3 (SHN3), as a potential target to prevent bone loss in RA. SHN3 expression in osteoblast-lineage cells is induced by proinflammatory cytokines. Germline deletion or conditional deletion of Shn3 in osteoblasts limits articular bone erosion and systemic bone loss in mouse models of RA. Similarly, silencing of SHN3 expression in these RA models using systemic delivery of a bone-targeting recombinant adenoassociated virus protects against inflammation-induced bone loss. In osteoblasts, TNF activates SHN3 via ERK MAPK-mediated phosphorylation and, in turn, phosphorylated SHN3 inhibits WNT/β-catenin signaling and up-regulates RANKL expression. Accordingly, knock-in of a mutation in Shn3 that fails to bind ERK MAPK promotes bone formation in mice overexpressing human TNF due to augmented WNT/β-catenin signaling. Remarkably, Shn3-deficient osteoblasts are not only resistant to TNF-induced suppression of osteogenesis, but also down-regulate osteoclast development. Collectively, these findings demonstrate SHN3 inhibition as a promising approach to limit bone loss and promote bone repair in RA.

rheumatoid arthritis | Schnurri-3 | WNT signaling | osteoblast | osteoclast

Significance

Rheumatoid arthritis (RA) is a chronic inflammatory disease that leads to focal destruction of articular bone and to systemic bone loss by activating osteoclastogenesis, resulting in osteopenia and osteoporosis. Despite currently available therapies for RA targeting inflammation and osteoclastogenesis, these agents are not able to fully prevent articular or systemic bone loss. Here, we demonstrate that Schnurri-3 (SHN3) is a potential target to prevent bone loss in RA. Our results show elevated levels of SHN3 in osteoblast-lineage cells under RA conditions and demonstrate that its deletion limits articular bone erosion and systemic bone loss in animal models of RA. Mechanistically, SHN3-deficient osteoblast lineage cells are not only resistant to TNF-induced suppression of osteogenesis, but also down-regulate osteoclast development.

Rheumatoid arthritis (RA) is a chronic inflammatory disease that leads to focal destruction of articular bone and to systemic bone loss, resulting in osteopenia and osteoporosis. Inflammation activates osteoclastogenesis, resulting in bone resorption (1, 2) while simultaneously suppressing the ability of osteoblasts to differentiate and build bone (3). Expression of secreted WNT/β-catenin antagonists including DKK1 (4), DKK2, SFRP1 (3), and SOST (5) is induced in RA synovial tissues. RA patients develop joint erosions soon after disease onset, while systemic bone loss is evident in the pre-RA period even prior to clinically apparent arthritis (6). Currently available therapies for RA target inflammation and osteoclastogenesis and are considered a breakthrough in treatment (7). However, while these agents prevent radiographic progression, they are not typically able to reverse existing joint erosions (8–10) or to fully prevent systemic bone loss.

Compared to the general population, RA patients have a twofold risk of osteoporosis and up to a threefold risk of hip fracture (11, 12). Most existing osteoporosis therapies, including bisphosphonates and anti-RANKL antibodies, target osteoclasts, but these agents do not cure osteoporosis and are limited by side effects including atypical femoral fractures and osteonecrosis of the jaw (13). Bone anabolic agents including intermittent parathyroid hormone (PTH) and parathyroid hormone-related protein (PTHrP) (14, 15) promote osteoblast function. However, these agents are limited in their use due to potential side effects and require daily injections (16). The anti-SOST antibody promotes osteoblast differentiation by enhancing WNT/β-catenin signaling, but this agent is associated with adverse cardiovascular events (17). Moreover, this antibody could worsen TNF-dependent inflammation in RA patients (5). Thus, therapeutic agents that prevent bone loss and promote healing of bone damage in RA, while limiting potential side effects, are needed.

The intracellular adaptor protein Schnurri-3 (SHN3, HIVEP3) inhibits WNT/β-catenin signaling in osteoblasts and suppresses bone formation (18). SHN3 function is intrinsic to osteoblasts, as osteoblast-specific deletion of Shn3 in mice results in a progressive increase in bone mass due to augmented osteoblast activity (18–21). Notably, the bone formed in these mice is mature lamellar bone with normal biomechanical properties (19) and Shn3 deficiency is not associated with phenotypes in nonskeletal tissues. Here we uncover a mechanism by which SHN3 regulates inflammation-induced bone loss in RA and show that SHN3 expression is up-regulated by the proinflammatory cytokines TNF plus IL-17A

in osteoblast-lineage cells. TNF also induces ERK-mediated phosphorylation of SHN3 in osteoblasts, resulting in suppression of WNT-mediated osteogenesis and upregulation of RANKL. Accordingly, *Shn3*-deficient osteoblasts are resistant to TNF-induced suppression of osteogenesis and down-regulate RANKL/OPG ratios. Germline deletion of *Shn3*, conditional deletion in osteoblasts, or adenoassociated virus (AAV)-mediated *Shn3* silencing, significantly limit systemic bone loss and articular bone erosion in mouse models of RA. Thus, silencing of SHN3 expression in osteoblasts may represent an innovative avenue for prevention of inflammation-induced bone loss in RA and other skeletal diseases of low bone mass.

Results

Osteoblast-Specific Upregulation of Shn3 in RA. In patients with RA, arthritic inflammation suppresses osteoblast-mediated bone formation, at least in part through upregulation of inhibitors of the WNT signaling pathway (3, 22). Schnurri-3 (SHN3) has been shown to suppress WNT/β-catenin signaling in osteoblasts (18). We demonstrate SHN3 expression by immunohistochemistry (IHC) in bone-lining osteoblasts and in tartrate-resistant acid phosphatase (TRAP)-expressing osteoclasts in synovial/bone tissues obtained from RA patients (Fig. 1*A*). *Shn3* mRNA expression is up-regulated in bone tissue, but not in synovial tissue, harvested from mouse models of RA: curdlan-treated SKG mice (23) and human TNF-transgenic mice (TNF-tg) (24) (Fig. 1 *B* and *C*), suggesting that bone-residing osteoblasts and/or osteoclast-lineage cells are major cell types demonstrating upregulation of SHN3 in inflammatory arthritis.

Multiple-transcriptome analyses revealed a strong association of SHN3 expression and signaling pathways of RA-related factors including TNF, IL-17A, IL-1β, IFNs, and Toll-like receptor ligands (Fig. 1*D*). We thus exposed human bone marrow-derived stromal cells (BMSCs, osteoblast precursors) to TNF, IL-17A, and TNF plus IL-17A and confirm previous findings (25) that human BMSCs isolated from RA patients are highly responsive to treatment with these cytokines, demonstrating an additive effect in the induction of *Shn3* mRNA expression (Fig. 1*E*). This is consistent with up-regulated expression of *Shn3* mRNA by TNF and TNF plus IL-17A in mouse osteoblast-lineage cells including calvarial osteoblasts (COB), BMSCs, and the osteocyte cell line (OCY454), demonstrating additive effects on *Shn3* induction in mouse COBs and BMSCs or a synergistic effect in mouse osteocytes (Fig. 1*F*). Of note, this response is specific to osteoblast-lineage cells, as *Shn3* mRNA was not up-regulated in preosteoclasts, monocytes, or B or T lymphocytes (Fig. 1*G*). Consistent with a previous study showing upregulation *Shn3* expression in fibroblast-like synoviocytes (FLS) of RA patients in response to TNF plus IL-17A (26), mouse FLS with these treatments also up-regulated *Shn3* expression (*SI Appendix*, Fig. S1*A*). However, there is no difference in expression levels in the synovium of SKG mice compared with wild-type mice (Fig. 1*C*). Notably, single-cell RNA sequencing analysis of the synovial tissues of RA patients shows that SHN3 expression in synovial cells, such as fibroblasts and monocytes, is comparable (*SI Appendix*, Fig. S1*B*). These results suggest that SHN3 expression in synovium might be sensitive to timing and/or duration of exposure to inflammatory cytokines.

Germline Deletion of Shn3 Limits Bone Loss in a Mouse Model of RA. To determine the role of SHN3 in bone loss in RA, mice with germline deletion of *Shn3* (*Shn3*$^{-/-}$) were crossed with SKG mice in which a mutation in the ZAP-70 protein alters signaling

through the T cell receptor with subsequent alteration of the T cell repertoire, increasing the number of peripheral autoreactive T cells (23). Onset of disease in SKG mice can be synchronized and augmented with systemic injection of 1,3-beta-glucan (curdlan) (27), and SKG mice reproducibly develop inflammation in the paws, induction of TNF, IL-17, IL-1, and IL-6 in synovium, and resulting in osteoclast-mediated joint destruction and reduced systemic bone density (28). Assessment of clinical inflammation and ankle thickness demonstrated little to no joint inflammation in control curdlan-treated BALB/c mice (Fig. 2*A*, black line) or in curdlan-treated *Shn3*$^{-/-}$ mice (Fig. 2*A*, green line). However, equivalent clinical inflammation is present in curdlan-treated SKG mice (Fig. 2*A*, blue line) and in curdlan-treated *Shn3*$^{-/-}$;SKG mice (Fig. 2*A*, red line). While histologic scoring shows a mild decrease in the degree of inflammatory infiltrates in inflamed ankle joints of curdlan-treated *Shn3*$^{-/-}$;SKG mice, immune cell populations including macrophages, monocytes, neutrophils, and B and T lymphocytes were comparable in the ankle joints of these mice (Fig. 2 *B–D*). The percentage of splenic cell populations was also comparable in *Shn3*$^{-/-}$;SKG mice compared with SKG mice (*SI Appendix*, Fig. S2), demonstrating that SHN3 function is minimal in both joint and splenic inflammation in this RA model.

Shn3$^{-/-}$;SKG mice display a significant decrease in articular bone erosion in inflamed joints compared to SKG mice (Fig. 2 *C* and *D*). Similarly, microCT analysis shows a marked decrease in erosion pits in joints of *Shn3*$^{-/-}$;SKG joints compared with SKG mice (Fig. 2*E*), suggesting that *Shn3* deletion protects articular bone from the erosions that result from joint inflammation in RA. Additionally, systemic bone loss is markedly reduced in arthritic SKG mice in the absence of SHN3, as shown by greater trabecular bone mass in femurs (Fig. 2*F*). While SKG mice demonstrate a 46% reduction of trabecular bone mass in the femur compared with WT control mice, only a 21% reduction is observed in femurs of *Shn3*$^{-/-}$;SKG mice compared with *Shn3*$^{-/-}$ mice. Accordingly, TRAP staining demonstrates that *Shn3* deletion in SKG mice results in a significant decrease in the number of TRAP$^+$ osteoclasts in femurs (Fig. 2*G*). In addition, immunohistochemistry for osteocalcin (OCN) reveals an increased number of OCN$^+$ mature osteoblasts in *Shn3*$^{-/-}$;SKG mice compared to SKG mice sufficient for SHN3 (Fig. 2*H*). This is consistent with elevated serum levels of osteocalcin, a marker of bone formation, and decreased levels of collagen cross-linked C-terminal telopeptide 1 (Ctx-1), a marker of bone destruction, in *Shn3*$^{-/-}$;SKG mice compared to SKG mice (Fig. 2*I*). These results demonstrate that *Shn3* deletion limits both arthritic articular bone erosion and systemic bone loss in long bones via increased osteogenesis and decreased osteoclastogenesis. Thus, SHN3 plays an important role in systemic and articular bone loss in this RA model.

Shn3-Deficient Osteoblasts Are Resistant to Inflammation-Induced Inhibition of Differentiation. To determine how *Shn3* deletion suppresses inflammation-induced bone loss in vivo, osteogenic differentiation of human BMSCs was assessed in the absence or presence of SHN3 following treatment with the RA-related cytokines TNF and IL-17A. While extracellular mineralization activity (late osteogenic marker) of human BMSCs expressing control shRNA (sh-Ctrl) is markedly reduced with treatment with TNF plus IL-17A, mineralization is largely intact in human BMSCs expressing SHN3 shRNA (sh-SHN3) despite cytokine treatment (Fig. 3*A*). Similarly, osteogenic differentiation of mouse BMSCs isolated from WT femurs was suppressed, whereas differentiation of cells from *Shn3*$^{-/-}$ femurs occurs normally in the presence of TNF and IL-17A, as shown
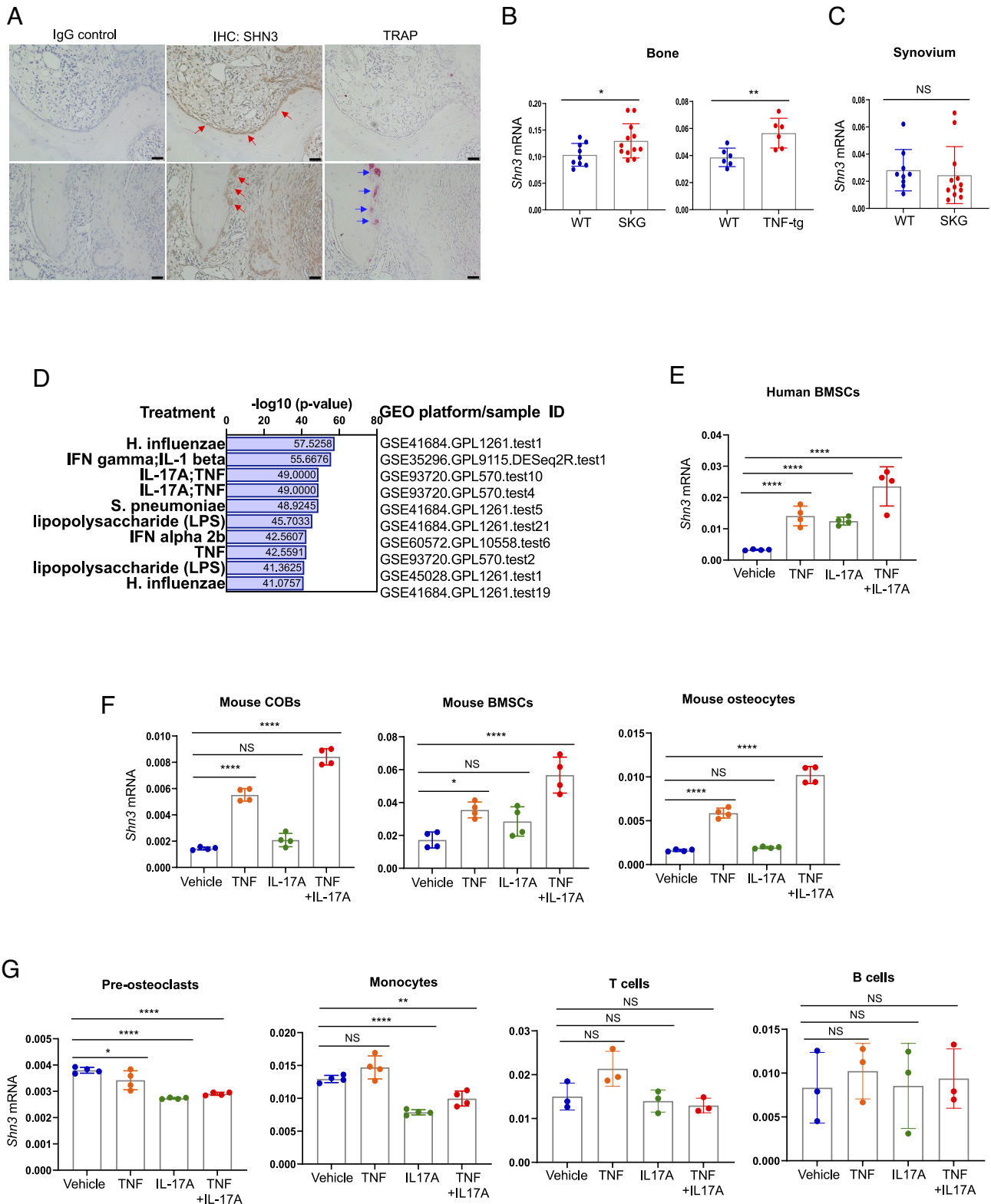
Fig. 1. SHN3 expression in osteoblasts is up-regulated in RA. (*A*) Immunohistochemistry (IHC) for *SHN3* in the inflamed metatarsal bones of RA patients (n = 5). IgG control antibody (*Left*) shows negative staining. Red arrows indicate staining for *SHN3* protein in osteoblasts lining the bone surface (*Mid*, *Top*). Staining for *SHN3* protein in osteoclasts (*Mid*, *Bottom*) is confirmed in a serial section stained for TRAP (blue arrows: *Right*, *Bottom*). (Scale bar = 50 μm.) (*B* and *C*) *Shn3* mRNA expression in the tibial bone and synovium in two mouse models of RA, SKG, and TNF transgenic (tg) mice and in synovium in SKG mice. There is a statistically significant increase in *Shn3* mRNA expression in the tibial bone of both SKG and TNF-tg mice compared with bone in nonarthritic wild-type (WT) littermate controls, but no difference in *Shn3* mRNA expression in synovium from SKG arthritic mice compared with WT nonarthritic mice (n = 6 ~ 12). (*D*) Match database analysis (>100,000 analyses) demonstrating the top 10 biological ligands associated with SHN3 expression. (*E* and *F*) Human bone marrow stromal cells (BMSCs, *E*), mouse calvarial osteoblasts (COBs, *F*), mouse BMSCs (*F*) and mouse osteocytes (OCY454, *F*) were treated with TNF, IL-17A or the combination for 6 h and *Shn3* mRNA expression was assessed by RT-PCR (n = 4). (*G*) Mouse bone marrow-derived monocytes (BMMs) were differentiated into preosteoclasts in the presence of M-CSF and RANKL for 3 d, then treated with TNF, IL-17A, or the combination for 6 h. Alternatively, undifferentiated BMMs or B or T cells isolated from mouse spleen were similarly treated. *Shn3* mRNA expression was assessed by RT-PCR (n = 3 ~ 4). Data shown in (*A*–*C*) and (*D*–*G*) are representative of three independent experiments. Values represent mean ± SD: NS, nonsignificant; *$P < 0.05$; **$P < 0.01$; ****$P < 0.0001$ using a two-tailed unpaired Student's *t* test for comparing two groups (*B* and *C*) or one-way ANOVA with Dunnett's multiple comparisons test (*E*–*G*).
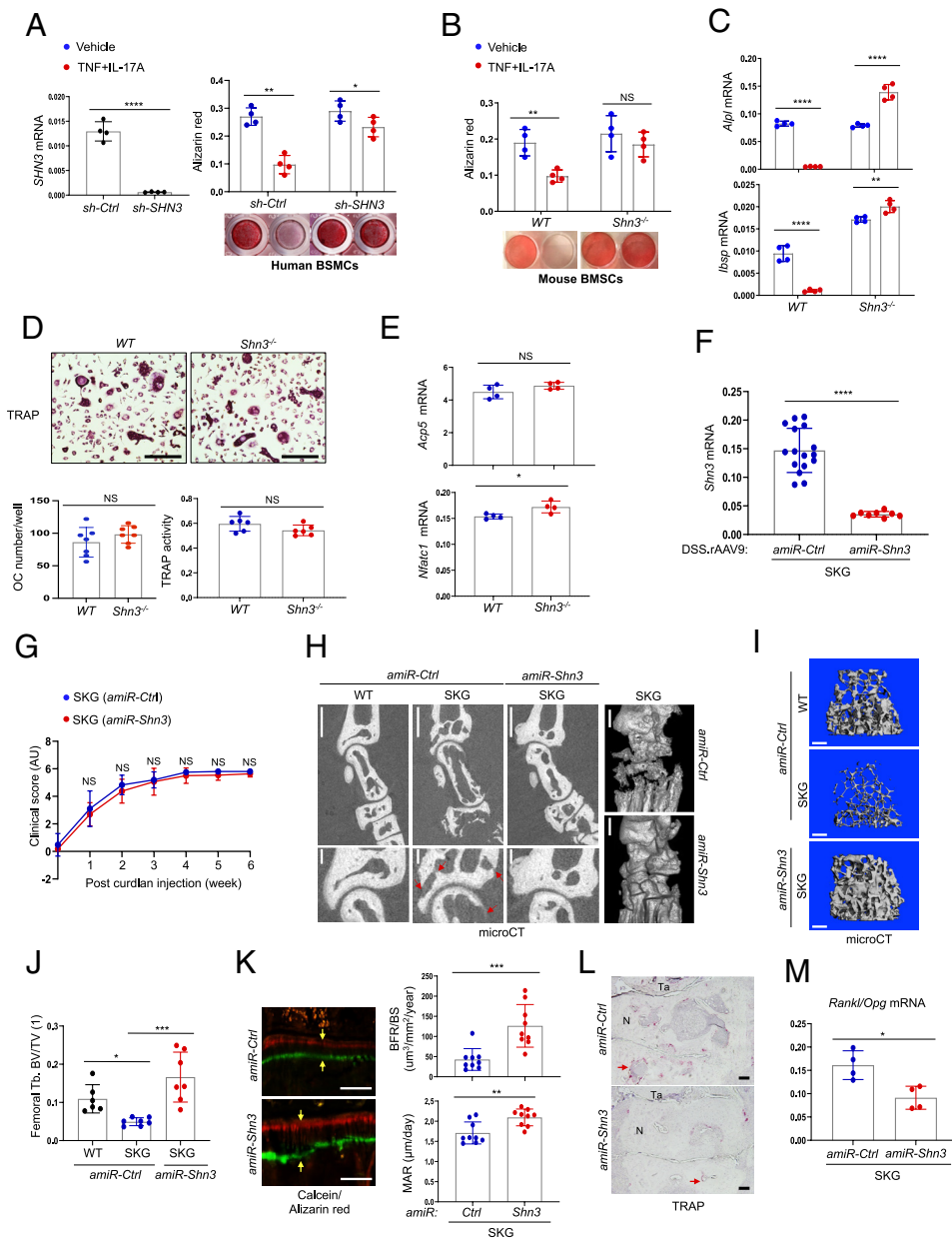
Fig. 2. SHN3 deletion inhibits inflammation-induced bone loss in SKG mice. (*A*) Ten-week-old WT (*Shn3*+/+), *Shn3*-/-, SKG, and *Shn3*-/-SKG mice were injected with curdlan. Ankle thickness and clinical joint inflammation were measured weekly. *WT* and *Shn3*-/- demonstrate no inflammation, while SKG and *Shn3*-/- SKG mice develop equivalent levels of inflammation. (n = 3 ~ 4: WT (*Shn3*+/+), *Shn3*-/- groups, n = 9 ~ 10: SKG, *Shn3*-/-SKG groups). (*B*) Flow cytometric analysis of immune cell from inflamed synovial tissues isolated from SKG and *Shn3*-/-SKG mice show equivalent percentages of immune cells (n = 3). (*C* and *D*) H&E- and TRAP-stained sections of inflamed ankles (*C*) and relative quantification of inflammation and erosion (*D*), demonstrating that *Shn3*-/-SKG mice are protected from articular erosion. Red arrows indicate TRAP+ osteoclasts. (Scale bars: *Left*, 200 μm; *Right*, 50 μm; Ta, talus; II, inflammatory infiltrates; N, navicular bone (n = 9~10/group).) (*E*) MicroCT images showing sagittal sections of inflamed ankles in SKG and *Shn3*-/-SKG mice, demonstrating fewer erosions in *Shn3*-/-SKG. Red arrows indicate sites of bone erosion. (Scale bars: *Top*, 400 μm; *Bottom*, 100 μm.) (*F*) MicroCT analysis showing trabecular bone in the femurs of SKG and *Shn3*-/-SKG. 3D reconstruction (*Top*) and relative quantification of trabecular bone volume/total volume (Tb. BV/TV, bottom) (n = 6/group). (Scale bars: 500 μm.) (*G* and *H*) Longitudinal femoral sections were immunostained for osteocalcin (OCN) or stained for TRAP (*G*) and relative quantification of TRAP+ osteoclasts per bone perimeter (*G*) and OCN+ osteoblasts (Ob) per bone perimeter (B. Pm) (*H*) is displayed. Red arrows indicate TRAP+ Ocs, blue arrows indicate OCN positive Obs (n = 3 ~ 5/group). (Scale bars: 50 μm.) (*I*) Serum levels of osteocalcin (OCN, *Left*) or cross-linked C-terminal telopeptide 1 (Ctx-I, *Right*) in SKG and Shn3-/-SKG mice 7 wk postinjection of curdlan as measured by ELISA (n = 7 ~ 12/group). Values represent mean ± SD: NS, nonsignificant; *P < 0.05; **P < 0.01; ****P < 0.0001 by a two-tailed unpaired Student's *t* test for comparing two groups (*A*, *B*, *D*, and *I*) or one-way ANOVA with Dunnett's multiple comparisons test (*F* and *H*).

by normal mineralization activity (Fig. 3*B*) and expression of osteogenic genes (Fig. 3*C*). These results demonstrate that SHN3 mediates TNF/IL-17A–induced suppression of osteogenesis. Of note, there were little to no changes in osteoclast numbers, TRAP activity, and osteoclast gene expression in bone marrow-derived monocytes (BMMs) isolated from *Shn3*-/- femurs compared to *WT* femurs (Fig. 3 *D* and *E* and *SI Appendix*, Fig. S3), suggesting that SHN3 function is dispensable for osteoclast differentiation. Thus, *Shn3* deficiency in osteoblasts, not osteoclasts, is responsible for suppression of inflammation-induced bone loss.

To confirm that *Shn3* deficiency in osteoblast-lineage cells inhibits inflammation-induced bone loss, *Shn3* expression was deleted in SKG mice using systemic delivery of a bone-targeting recombinant adenoassociated virus (rAAV) vector carrying an artificial miRNA that silences expression of *Shn3* (amiR-Shn3). Previously,

rAAV9 was identified as a highly effective serotype for transduction of osteoblast-lineage cells in vitro and in vivo, and a novel AAV9 capsid was further developed to improve targeting of skeletal tissues by grafting the bone-targeting peptide motif (Asp-Ser-Ser)$_6$ onto the VP2 capsid protein (**DSS.rAAV9**) (29). SKG mice were injected intravenously (IV) with DSS.rAAV9 carrying *egfp*, *amiR-Ctrl*, or *amiR-Shn3* 2 wk prior to curdlan treatment (*SI Appendix*, Fig. S4*A*). Six weeks later, AAV transduction in the femur and inflamed ankle was assessed by EGFP expression using fluorescence microscopy. Immunofluorescence analysis in the inflamed ankle shows EGFP expression in a subset of OCN+ mature osteoblasts and Cathepsin K (CTSK)+ mature osteoclasts, but not in CD248+ fibroblast-like synoviocytes (FLS), demonstrating the ability of DSS.rAAV9 to transduce osteoblasts and osteoclasts, but not FLS (*SI Appendix*, Fig. S4*B*). Additionally, knockdown efficiency of *Shn3* in

Fig. 3. SHN3 deletion protects osteoblasts from inflammation-induced suppression of differentiation. (*A*) Human BMSCs were transduced with lentivirus expressing control (sh-Ctrl) or SHN3 (sh-SHN3) shRNA and cultured under osteogenic conditions in the presence or absence of TNF plus IL-17A. After 12 d, *SHN3* knockdown as assessed by RT-PCR (*Left*) and mineralization activity was quantified using alizarin staining (*Right*, n = 4). (*B* and *C*) Mouse *Shn3*$^{+/+}$ or *Shn3*$^{-/-}$ BMSCs were cultured under osteogenic conditions in the presence or absence of TNF plus IL-17A. Mineralization activity (*B*) and expression of the osteoblast differentiation markers *Alpl* and *Ibsp* (*C*) were assessed by alizarin red staining at day 18 and by RT-PCR at day 12 of culture (n = 4). (*D* and *E*) Mouse *Shn3*$^{+/+}$ or *Shn3*$^{-/-}$ BMMs were cultured under osteoclast differentiation conditions in the presence of TNF plus IL-17A. (*D*) TRAP-stained osteoclasts (*Top*) and quantification of multinucleated osteoclasts (*Bottom, Left*) and TRAP activity (*Bottom, Right*) in *Shn3*$^{+/+}$ or *Shn3*$^{-/-}$ BMMs differentiated to osteoclasts. (*E*) Expression of *Acp5* and *Nfatc1* mRNA in *Shn3*$^{+/+}$ or *Shn3*$^{-/-}$ BMMs differentiated to osteoclasts (n = 4 ~ 6). (Scale bars: *D*, 200 μm.) (*F–M*) SKG mice were treated via i.v. injection with DSS.rAAV9 carrying *amiR-Ctrl* or *amiR-Shn3* (5 × 10^{13} vg/kg). (*F*) 7 wk postinjection, *Shn3* mRNA in tibial bone was assessed by RT-PCR (n = 4). (*G*) Clinical joint inflammation scores demonstrated no difference in inflammation between *amiR-Ctrl* and *amiR-Shn3*-treated mice (n = 4 ~ 5/group). (*H*) MicroCT images showing sagittal sections of inflamed ankles from *amiR-Ctrl*-treated WT and SKG mice and *amiR-Shn3*-treated SKG mice. Red arrows indicate bone erosion sites. (Scale bars: *Top Left*, 400 μm; *Top Right*, 200 μm; *Bottom*, 100 μm.) (*I* and *J*) MicroCT analysis showing femoral trabecular bone mass from *amiR-Ctrl*-treated WT and SKG mice and *amiR-Shn3*-treated SKG mice, 3D reconstruction (*I*) and quantification of trabecular bone mass from *I* (*J*). (*I*, n = 6 ~ 7/group). (Scale bars: 500 μm.) (*K*) Representative images of calcein/alizarin red labeling. Yellow arrows indicate the distance between calcein and alizarin labels (*Left*). Histomorphometric quantitation of bone formation rate (BFR)/bone surface (BS) and mineral apposition rate (MAR) (*Right*), showing increases in BFR/BS and MAR in amiR-Shn3-treated mice (n = 9). (Scale bars: 50 μm.) (*L*) TRAP-stained sections of inflamed ankles in *amiR-Ctrl* and *amiR-Shn3*-treated SKG mice. Red arrows indicate TRAP$^+$ osteoclasts. (Scale bars: 100 μm.) (*M*) *Rankl/Opg* mRNA ratios in tibial bone RNA from *amiR-Ctrl* and *amiR-Shn3*-treated SKG mice shows a decrease in the ratio in *amiR-Shn3*-treated mice (n = 4). Values represent mean ± SD: NS, nonsignificant; *$P < 0.05$; **$P < 0.01$; ***$P < 0.001$; ****$P < 0.0001$ by a two-tailed unpaired Student's t test for comparing two groups (*A–G, J, K,* and *M*).

AAV-treated tibial bones was validated by RT-PCR (Fig. 3*F*). As shown by clinical joint inflammation scores (Fig. 3*G*), joint inflammation in SKG mice is comparable following treatment with *amiR-Ctrl* or *amiR-Shn3*. This is consistent with flow cytometric analysis showing equivalent numbers of myeloid and lymphoid cell populations in *amiR-Shn3*-expressing splenic cells compared to *amiR-Ctrl*-expressing splenic cells (*SI Appendix,* Fig. S4C), demonstrating that AAV-mediated silencing of *Shn3* does not affect inflammation. As expected, inflammation in *amiR-Ctrl*-expressing SKG mice induces both articular and cortical bone erosion in inflamed ankles and midfoot bones compared with nonarthritic WT controls treated with *amiR-Ctrl* (Fig. 3*H*) and a significant decrease in trabecular bone mass in the femur (Fig. 3 *I* and *J*), respectively. Remarkably, these skeletal consequences are prevented by a single IV injection of DSS.rAAV9.*amiR-Shn3* in SKG mice, demonstrating that protection from bone loss by AAV-mediated silencing of

SHN3 occurs even in the presence of comparable levels of inflammation. Additionally, in vivo osteoblast activity is increased in SKG femoral trabecular bone expressing *amiR-Shn3* relative to *amiR-Ctrl*, as shown by the greater mineral apposition rate (MAR) and bone formation rate (BFR) (Fig. 3*K*). Furthermore, compared to *amiR-Ctrl*-expressing ankles, *amiR-Shn3*-expressing ankles display a decrease in areas with TRAP$^+$ osteoclasts marking articular erosion sites (Fig. 3*L*). Additionally, the number of TRAP$^+$ osteoclasts (*SI Appendix,* Fig. S5), *Rankl* mRNA levels (*SI Appendix,* Fig. S6A), and *Rankl/Opg* mRNA ratio (Fig. 3*M*) were markedly decreased in the femurs expressing *amiR-Shn3 relative to amiR-Ctrl*. These findings suggest that the downregulation of the *Rankl/Opg* mRNA ratio may be responsible for the decreased osteoclast development in these mice, since *Shn3*-deficient osteoclasts differentiate normally in vitro (Fig. 3 *D* and *E*). These results demonstrate that systemic delivery of DSS.AAV9.*amiR-Shn3* reduces *Shn3* expression in osteoblast

lineage cells, augments osteoblast function, and reduces osteoclast development, suppressing inflammation-induced bone loss in arthritic SKG mice without any alteration in inflammation. Thus, the DSS.rAAV9.*amiR-shn3* vector may be useful for the prevention of RA-associated bone loss.

Osteoblast-Specific Deletion of Shn3 Limits Bone Loss in K/BxN Serum Transfer Arthritis, a Mouse Model of RA Driven by IL-1β. K/BxN serum transfer arthritis (STA) is an established model of RA. Mice with STA develop spontaneous arthritis that mimics human RA, with leukocyte invasion in joints, pannus formation, cartilage destruction, and bone erosion (30, 31). To test whether osteoblast-specific deletion of *Shn3* can prevent articular bone erosion in this model, *Shn3* was conditionally deleted in osteoblast-lineage cells by crossing mice bearing a floxed allele of *Shn3* (*Shn3^fl/fl^*) with Prx1-Cre mice (*Shn3^Prx1^*), which targets the limb-specific mesenchyme (32). These mice were then injected intraperitoneally (IP) with arthritic K/BxN serum. Deletion of *Shn3* was confirmed in the tibial RNA of *Shn3^Prx1^* mice (Fig. 4*A*). Joint inflammation peaks approximately 10 days post initial injection of serum in both *Shn3^fl/fl^* and *Shn3^Prx1^* mice, as shown by clinical joint inflammation and ankle thickness scores (Fig. 4*B*). This is consistent with a histologic analysis showing that inflammatory infiltrates in inflamed ankles of these mice are comparable (Fig. 4 *C* and *D* and *SI Appendix*, Fig. S7), suggesting that osteoblast-specific deletion of *Shn3* does not affect joint inflammation in this model. However, arthritic *Shn3^Prx1^* mice display a significant decrease in articular bone erosion (Fig. 4 *C* and *D*), in which the number of TRAP⁺ osteoclasts is reduced in pannus tissue, while the number of OCN⁺ osteoblasts at erosion sites is increased (Fig. 4*E*) compared with control *Shn3^fl/fl^* mice. In support of this finding, *Rankl* mRNA levels and the *Rankl/Opg* mRNA ratio are decreased in *Shn3^Prx1^* mice (Fig. 4*F* and *SI Appendix*, Fig. S6*B*). Expression of mRNA for the WNT antagonist SFRP1 is also markedly reduced in the absence of *Shn3,* while expression of mRNA for other WNT antagonists, DKK1 and SOST, are unchanged (Fig. 4*F*). In the STA model, SFRP1 is up-regulated by inflammation, whereas DKK1 levels are unchanged (3). These results suggest that downregulation of the *Rankl/Opg* mRNA ratio and SFRP1 may contribute to reducing the number of osteoclasts in the pannus while increasing the number of osteoblasts.

Osteoblast-Specific Deletion of Shn3 Limits Bone Loss in a TNF-Driven Mouse Model of RA. Mice with overexpression of human TNF (TNF-tg) display an erosive polyarthritis and systemic osteoporosis mimicking that observed in RA (24). To test whether osteoblast-specific deletion of *Shn3* can prevent bone loss by TNF-driven inflammation, *Shn3^Prx1^* mice were crossed with TNF-tg mice. While TNF-driven joint inflammation was comparable, *Shn3^Prx1^ TNF-tg* mice showed a significant decrease in articular bone erosions and TRAP⁺ osteoclast area compared to *Shn3^fl/fl^ TNF-tg* mice (Fig. 4 *G–J*). Notably, in vitro osteoclast differentiation and resorption activity of BMMs isolated from *Shn3^Prx1^ TNF-tg* mice were largely intact, as shown by TRAP activity and staining, resorption pit assays, and expression of osteoclast differentiation genes (*SI Appendix*, Fig. S7). Since *Rankl* mRNA levels and the *Rankl/Opg* mRNA ratio in *Shn3^Prx1^ TNF-tg* bones were markedly reduced compared with *Shn3^fl/fl^ TNF-tg bones* (Fig. 4*K* and *SI Appendix*, Fig. S6*C*), these results suggest that the downregulation of the *Rankl/Opg* ratio in *Shn3^Prx1^* osteoblasts, not an impaired osteoclastogenic potential of *Shn3^Prx1^ TNF-tg* BMMs, is responsible for the reduced number of osteoclasts in inflamed ankles. *Shn3^fl/fl^ TNF-tg* femurs displayed a significant decrease in trabecular bone mass, and TNF-driven bone loss was partially prevented by osteoblast-specific deletion of *Shn3* (Fig. 4*L*). These results demonstrate that osteoblast-specific deletion of *Shn3* is effective for suppression of both joint and systemic bone loss in TNF-driven inflammatory conditions, in part by reducing osteoclast development. Taken together, SHN3 function in osteoblasts is important for regulating articular bone erosion in inflamed joints and systemic bone loss in long bones in the setting of arthritis, while SHN3 is dispensable for controlling immune responses in these RA models. Of interest is the fact that *Shn3* mRNA is also produced by marrow adipogenic lineage precursor cells (*SI Appendix*, Fig. S8), which could contribute to RANKL expression in vivo.

SHN3 Mediates TNF-Induced Osteogenic Suppression and RANKL Production. To gain insights into the mechanism by which SHN3 mediates inflammation-induced bone loss, phosphorylation levels of SHN3 in osteoblasts were determined following TNF or IL-17A stimulation at different time points. Immunoblot analysis demonstrates that phosphorylation of SHN3 and ERK, p38, and JNK MAPKs peaks at 15 min poststimulation by TNF (Fig. 5*A*) while the phosphorylation levels are unchanged by IL-17A stimulation alone (*SI Appendix*, Fig. S9*A*). Notably, HEK293 cells are not responsive to TNF to induce SHN3 phosphorylation (*SI Appendix*, Fig. S9*B*), suggesting that the phosphorylation events might be specific to TNF stimulation in osteoblasts. Since the MAPK pathways (ERK, JNK, and p38) are major mediators of TNF signaling transduction via phosphorylation (33) and among them, ERK MAPK binds to SHN3 in osteoblasts (18), we hypothesized that ERK MAPK may act as an upstream kinase of SHN3 in TNF signaling. Accordingly, TNF-induced phosphorylation of SHN3 is markedly reduced when treated with an ERK inhibitor, but not with inhibitors of p38 or JNK (Fig. 5*B*). Likewise, an in vitro kinase analysis using recombinant ERK2 MAPK (rERK2) and SHN3 (rSHN3, 50-930 aa) indicated ERK MAPK as a potential upstream kinase of SHN3 (Fig. 5*C*). Using a protein motif search program, we identified a putative MAPK-binding domain (the D-domain; PP**KKK**RARA, 884-892 aa) in the BAS domain of mouse SHN3 protein (Fig. 5 *D*, *Top*). Substitution of three lysines to alanines (SHN3-KA) fails to bind to ERK MAPK and significantly reduces the ability of ERK MAPK to phosphorylate SHN3 (Fig. 5 *D*, *Bottom*). Additionally, phosphospectrometry analysis using rERK2 and rSHN3 reveals that rERK2 phosphorylates rSHN3 at two serines (810 and 811 aa), one threonine (851 aa), and two serines (911 and 913 aa) (Fig. 5 *D*, *Top*). Only when these phosphorylation sites are all substituted to alanines (SHN3-STA), ERK-induced phosphorylation of SHN3 is markedly reduced (Fig. 5 *D*, *Bottom*), confirming that ERK-mediated phosphorylation of SHN3 occurs at S810/S811/T851/S911/S913. Of note, a significant difference of TNF-induced activation of downstream mediators, including the MAPK pathways and NF-κB signaling (34), was barely detectable in WT and SHN3-deficient osteoblasts (*SI Appendix*, Fig. S9*C*).

To determine the contribution of ERK-induced phosphorylation of SHN3 to TNF-induced osteogenic suppression, SHN3 constructs expressing WT (SHN3-WT), ERK-binding defective mutant (SHN3-ΔD, SHN3-KA), or ERK-phosphorylation defective mutant (SHN3-STA) were transduced to *Shn3*-deficient BMSCs expressing human TNF (*Shn3^Prx1^ TNF-tg*) and cultured under osteogenic conditions. While reconstitution of SHN3-WT inhibits ALP activity and expression of osteogenic genes, there is little to no inhibition by expression of SHN3-ΔD, SHN3-KA, or SHN3-STA (Fig. 5 *E* and *F*), demonstrating that ERK-induced phosphorylation is required for the ability of SHN3 to suppress osteogenesis upon TNF stimulation. To test this in vivo, mice
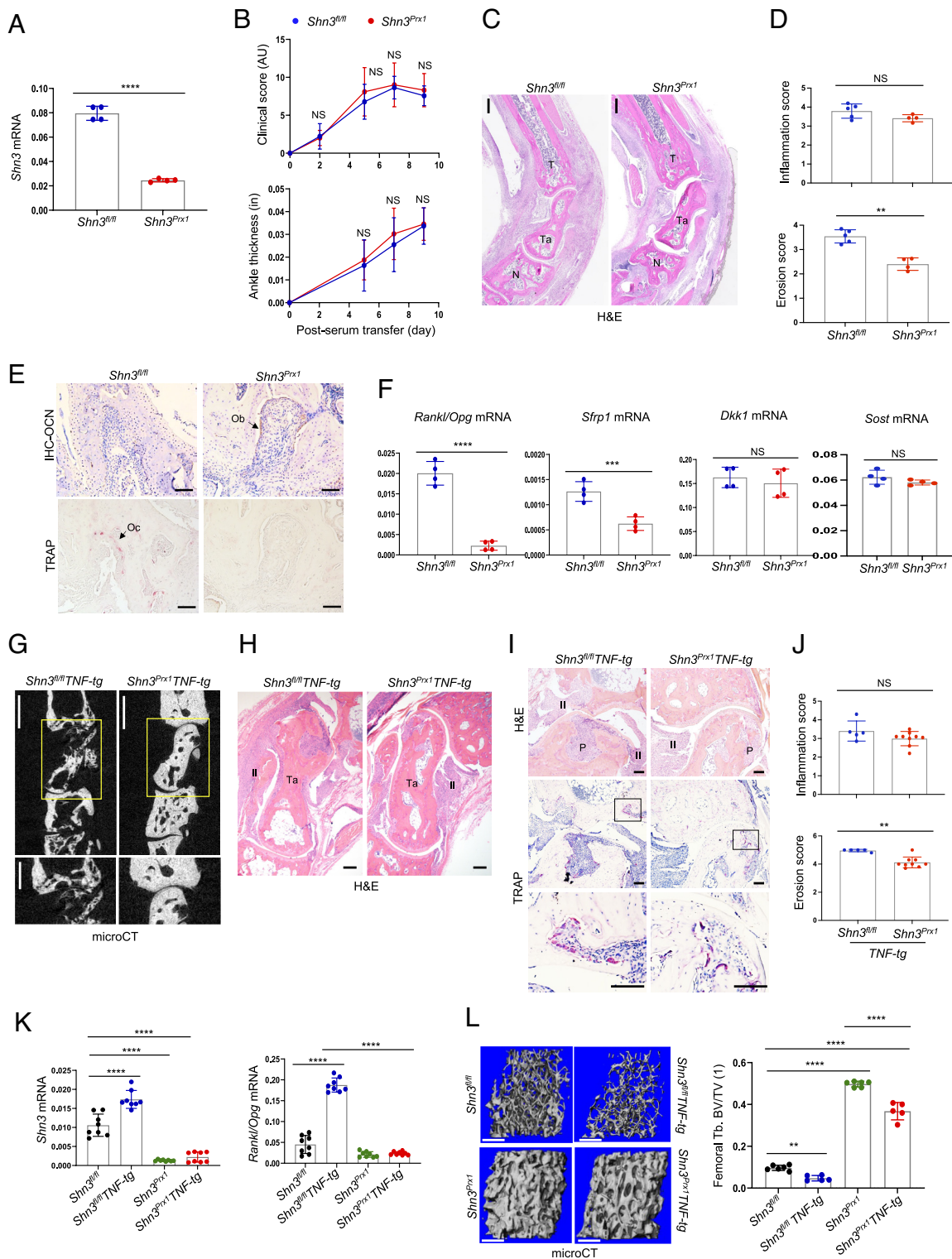
Fig. 4. Osteoblast-specific deletion of SHN3 inhibits articular erosion and systemic bone loss in two models of RA. (A–F) **Serum transfer arthritis**: Five-week-old *Shn3^fl/fl* and *Shn3^Prx1* mice were induced with serum transfer arthritis. (A) *Shn3* deletion as assessed by RT-PCR in tibial bones (n = 4). (B) Clinical inflammation (*Top*) and ankle thickness (*Bottom*) scores show no difference (n = 5 ~ 7/group). (C) Sagittal H&E-stained sections of inflamed ankles. (Scale bars: 500 µm.) T: tibia, Ta: talus, N: navicular bone. (D) Histologic quantification of inflammation and erosion show no difference in inflammation, but protection from erosion in *Shn3^Prx1* mice compared with *Shn3^fl/fl* mice (n = 4 ~ 5/group). (E) Tibio-talar joint sections were immunostained for OCN (*Top*) or TRAP (*Bottom*). Ob, osteoblast; Oc, osteoclast. (Scale bars: 100 µm.) (F) *Rankl/Opg* mRNA ratios and mRNA levels of *Sfrp1*, *Dkk1*, and *Sost* in *Shn3^fl/fl* and *Shn3^Prx1* tibias (n = 4). (G–L) **TNF-tg model of RA**. (G) MicroCT sagittal sections of inflamed ankles (boxes indicate the talus bone) and (H) H&E-stained sections of inflamed midfoot in 12-wk-old *Shn3^fl/fl*TNF-tg and *Shn3^Prx1*TNF-tg mice show protection from erosion in the *Shn3^Prx1*TNF-tg mice. (Scale bars: (G) *Top*, 400 µm; *Bottom*, 200 µm; (H) 250 µm). (I and J) H&E- (*Top*, I) and TRAP- (*Middle & Bottom*, I) stained sections of inflamed tibio-talar joints and (J) histologic quantification of inflammation (*Top*) and erosion (*Bottom*) show protection from articular erosion in *Shn3^Prx1*TNF-tg mice compared with *Shn3^fl/fl* mice (J, n = 5 ~ 9). (Scale bars: *Top*, 250 µm; *Middle*, 250 µm; *Bottom*, 100 µm). (K) *Shn3* mRNA levels in tibial bones confirm *Shn3* deletion (*Left*) and *Rankl/Opg* ratios show a significant decrease in *Rankl/Opg* mRNA levels in *Shn3^Prx1* and *Shn3^Prx1*TNF-tg mice compared with *Shn3^fl/fl*TNF-tg mice (n = 8). (L) MicroCT 3D reconstruction images of femoral trabecular bone mass showing protection from systemic bone loss in *Shn3^Prx1*TNF-tg mice (*Left*, Scale bars: 500 µm). Quantification of trabecular BV/TV shows significant increases in *Shn3^Prx1* and *Shn3^Prx1*TNF-tg mice compared with *Shn3^fl/fl* TNF-tg mice (*Right*, n = 5 ~ 6/group) Ta: talus, II: inflammatory infiltration, P: pannus. Values represent mean ± SD: NS, nonsignificant; **$P < 0.01$; ***$P < 0.001$; ****$P < 0.0001$ by a two-tailed unpaired Student's *t* test for comparing two groups (A–D, F, and J) or one-way ANOVA with Dunnett's multiple comparisons test (K and L).

bearing a knock-in allele of SHN3-KA in the endogenous *shn3* locus ($Shn3^{KA/KA}$) were crossed with *TNF-tg* mice. Compared to *TNF-tg* mice, $Shn3^{KA/KA}TNF-tg$ mice display a significant reduction in both articular bone erosions in inflamed ankles (Fig. 5*G*) and trabecular bone loss in the femur (Fig. 5*H*), suggesting that ERK-induced phosphorylation of SHN3 is critical for TNF-driven bone loss. Consistent with our findings that *Shn3*-deficient BMSCs reconstituted with the SHN3-KA mutant are resistant to osteogenic suppression by TNF (Fig. 5 *E* and *F*), in vivo osteoblast activity was increased in the femur of $Shn3^{KA/KA}TNF-tg$ mice relative to *TNF-tg* mice, as shown by the greater MAR and BFR (Fig. 5*I*). These results demonstrate the importance of ERK-induced phosphorylation of SHN3 in osteogenic suppression in a TNF-driven model of RA.

Despite a previous study showing paradoxical roles of TNF in Wnt/β-catenin signaling in osteoblasts (35), our data show a significant reduction in mRNA levels of the β-catenin target gene *Axin2* in the long bone of *TNF-tg* mice. This reduction is prevented by osteoblast-specific deletion of *Shn3* ($Shn3^{Prx1}TNF-tg$, *SI Appendix*, Fig. S9*D*), suggesting that TNF stimulation suppresses Wnt/β-catenin signaling in osteoblasts, which may be mediated by SHN3. Similarly, a luciferase assay using a β-catenin reporter gene (Topflash-Luc) shows enhanced β-catenin transcription activity in BMSCs isolated from $Shn3^{KA/KA}$ mice relative to $Shn3^{+/+}$ mice following TNF treatment (Fig. 5*J*). Expression of the β-catenin target gene *Lef1* (Fig. 5*K*) and β-catenin protein (Fig. 5*L*) in the long bones of $Shn3^{KA/KA}TNF-tg$ mice is also markedly increased, suggesting that ERK-induced phosphorylation of SHN3 is critical for TNF-induced suppression of Wnt/β-catenin signaling in osteoblasts. In addition to enhanced Wnt/β-catenin signaling, $Shn3^{KA/KA}TNF-tg$ mice show a significant decrease in numbers of TRAP⁺ osteoclasts in long bones (Fig. 5*M*). Accordingly, *Rankl* mRNA levels and the *Rankl/Opg* mRNA ratio are markedly decreased in $Shn3^{KA/KA}$ BMSCs relative to *WT* BMSCs following TNF treatment (Fig. 5*N* and *SI Appendix*, Fig. S7*D*). Conversely, *Rankl* mRNA levels and the *Rankl/Opg* mRNA ratio in $Shn3^{Prx1}$ BMSCs are up-regulated by reconstitution with SHN3-WT, not with SHN3-KA, or SHN3-STA, following TNF treatment (Fig. 5*O* and *SI Appendix*, Fig. S9*E*), suggesting that ERK-induced phosphorylation downstream of TNF is critical for SHN3-mediated expression of *Rankl* in osteoblasts. Taken together, ERK-induced phosphorylation of SHN3 is likely to be a key determinant of suppression of Wnt/β-catenin signaling and RANKL production by TNF stimulation, resulting in decreased osteogenesis and increased osteoclastogenesis, respectively. Thus, inhibition of SHN3 phosphorylation or expression would be an attractive approach to prevent TNF-dependent bone loss in RA by promoting bone formation and reducing bone resorption, simultaneously.

Discussion

RA leads to osteoclast-mediated focal destruction of articular bone and is associated with significant inflammation-induced systemic bone loss. In addition, inflammation in RA inhibits the differentiation and function of osteoblasts, at least in part through the upregulation of inhibitors of the WNT signaling pathway (3, 4, 22), contributing to net systemic bone loss and leading to a lack of healing of articular erosions. We have previously shown that inducible knockdown of the intracellular adaptor protein SHN3 in adult mice results in bone accrual and that SHN3 down-regulates WNT/β-catenin signaling by blocking ERK-mediated stabilization of β-catenin (18). Thus, we considered that SHN3 might be an important target for the protection from bone loss in RA.

Here, we demonstrate that SHN3 expression is up-regulated in osteoblast-lineage cells by the proinflammatory cytokines TNF

and IL-17A that contribute to RA pathogenesis. We investigated the role of SHN3 in bone in three animal models of RA with different pathogenic mechanisms, mice with K/BxN serum transfer arthritis, SKG mice and TNF-tg mice, and show that deletion of *Shn3* results in protection from articular bone erosion as well as protection from systemic trabecular bone loss in all three models. Notably, the effects of TNF on SHN3 expression and activation are restricted to osteoblast-lineage cells. In line with these findings, while SHN3 deficiency ameliorated joint damage and systemic bone loss in TNF-tg mice, there was no effect on TNF-dependent inflammation.

Mechanistically, TNF stimulation phosphorylates SHN3 via the ERK MAPK, resulting in suppression of osteogenic differentiation and upregulation of RANKL expression (*SI Appendix*, Fig. S9*E*). Lack of the ability to phosphorylate SHN3 (SHN3-STA) or impaired binding to ERK (SHN3-KA) abrogates the ability of SHN3 to inhibit osteogenesis and limits RANKL expression. Accordingly, mice harboring the knock-in allele of *Shn3* (SHN3-KA) display an increase in WNT/β-catenin signaling, osteogenesis, and bone formation in the setting of TNF-induced inflammation, while decreasing osteoclast development due to downregulation of RANKL expression. Similar to the secreted WNT antagonists SOST (5) and DKK1 (4), SHN3 inhibition mitigates both articular bone erosions and systemic bone loss in part via uncoupling events between osteoblasts and osteoclasts. Osteoblast-specific deletion of *Shn3* promotes bone formation due to enhanced WNT/β-catenin signaling while reducing osteoclast-mediated bone resorption.

In contrast to previous studies showing the importance of SHN3 in activation of macrophages and T lymphocytes (36, 37), SHN3 in immune cells appears not to be critical for the generation of inflammatory arthritis in the mouse models of RA. Moreover, the function of SHN3 appears to be dispensable for immune responses in RA conditions as there was little to no changes in systemic inflammation and synovitis in the absence of SHN3. The secreted protein SOST interferes with the engagement of WNT ligands with the WNT receptor Frizzled by binding to low-density lipoprotein receptor-related proteins 5 and 6 (LRP5/6), suppressing WNT-induced osteogenesis and bone formation (38). However, SOST blockade worsened inflammation in TNF-tg mice, since SOST also inhibits TNF-induced activation of p38 MAPK and NF-κB through the WNT coreceptor LRP6 (5). Thus, the use of SOST antagonists may well be problematic in the setting of inflammatory arthritis that is driven by TNF. We show that, unlike in the case of SOST, TNF-induced activation of p38 MAPK and NF-κB is unchanged in *Shn3*-deficient osteoblasts.

Collectively, these properties make SHN3 a potential target for the prevention of inflammatory bone loss in RA. Knockdown of *Shn3* expression in osteoblasts is also an attractive approach to promote bone formation in the arthritic setting, especially given that a modest 30% reduction of *Shn3* mRNA levels results in a >50% increase in relative trabecular bone mass (18). AAV vectors have been considered for use in gene therapy due to their high-transduction efficiency, long-term expression, relatively low postinfection immunogenicity in animals and, importantly, no induction of human disease (39, 40). Since high levels of AAV-delivered shRNAs can induce cytotoxicity by perturbing the RNAi machinery or exhibit significant off-target silencing (41, 42), in this study the guide strand of a small silencing RNA of *shn3* was embedded into the mouse miR-33-derived miRNA scaffold (*amiR-Shn3*) to limit shRNA-related toxicity. This modification enabled efficient gene knockdown, while reducing off-target silencing by ten-fold compared to conventional shRNA
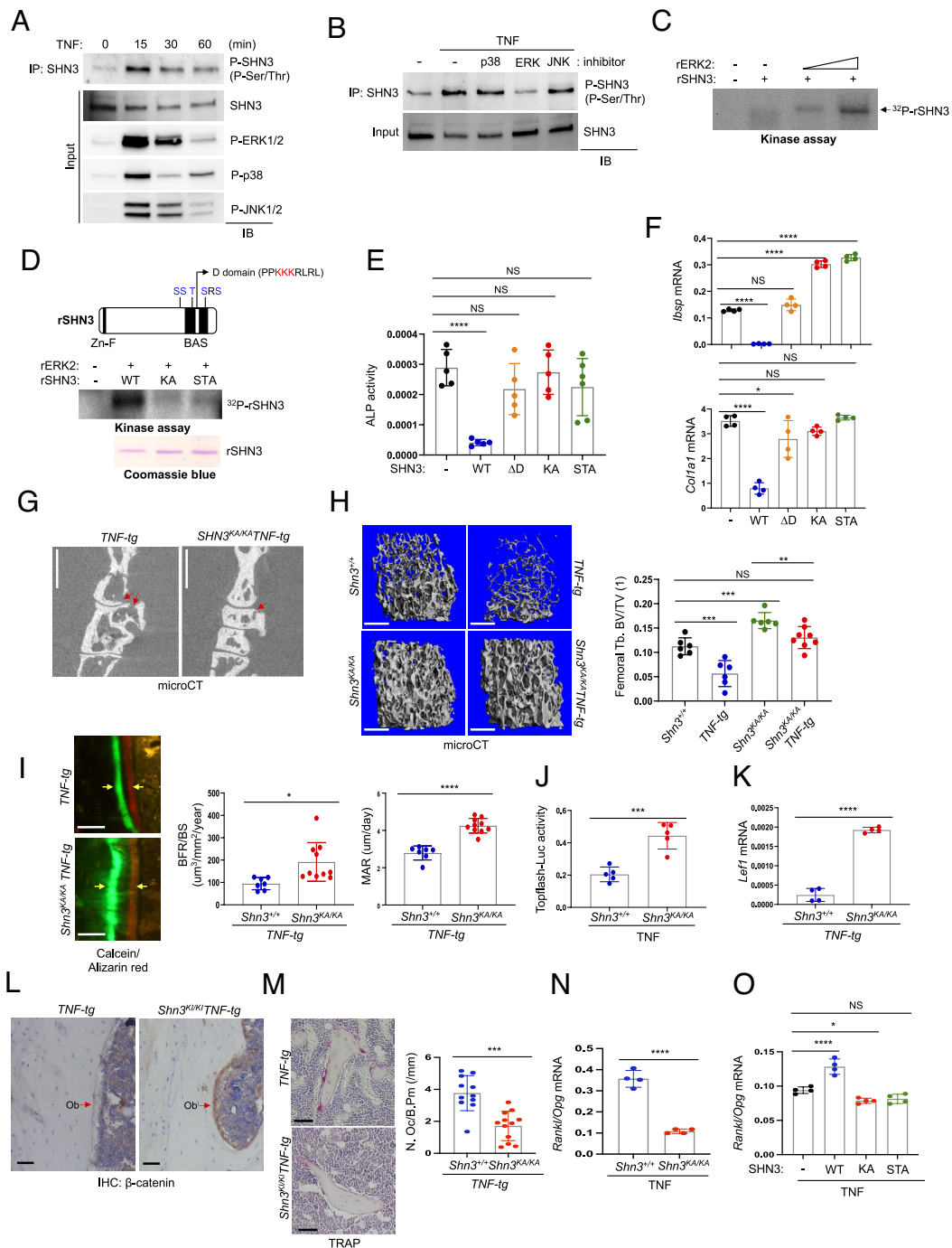
Fig. 5. ERK-induced phosphorylation of SHN3 is required for TNF-induced bone loss. (*A* and *B*) C3H10T1/2 cells expressing Flag-Shn3 were stimulated with TNF at different time points (*A*). Cells were pretreated with an inhibitor of p38, ERK, or JNK MAPK for 30 min, then stimulated with TNF for 15 min (*B*). Cell lysates were immunoprecipitated with Flag-conjugated agarose and immunoblots of pre-IP cell lysates with anti-phospho-serine/threonine antibody. Input indicates the immunoblots of pre-IP cell lysates with the indicated antibodies. (*C*) A cell-free kinase assay using recombinant ERK2 (rERK2) and His-SHN3 (rSHN3, p.50-936 aa) demonstrates ERK-induced phosphorylation of SHN3. (*D*) Schematic diagram showing SHN3 phosphorylation sites by ERK MAPK (*Top*, p.630-936 aa of rSHN3). A cell-free kinase assay using rERK2 and rSHN3s (WT, KA, STA) was performed, demonstrating ERK-induced phosphorylation of SHN3 at S810/S811/T851/S911/S913 via the interaction at K886/K887/K888 (*Bottom*). S810/S811/T851/S911/S913 (STA, ERK-phosphorylation defective mutant) or K886/K887/K888 (KA, ERK-binding defective mutant) were substituted to alanine. Coomassie blue staining indicates loading control of rSHN3. Zn-F, zinc finger domain; BAS, basic-, acidic-, and serine-rich region. (*E* and *F*) BMSCs were isolated from *Shn3^{Prx1}TNF-tg* mice, reconstituted with SHN3 proteins (WT, ΔD, KA, STA) via lentivirus-mediated delivery, and cultured under conditions of osteogenic differentiation. ALP activity (*E*) and expression of *Ibsp* and *Col1a1* (*F*) were assessed at day 6 of culture. ΔD: D domain deletion. (*E*, n = 5; *F*, n = 4). (*G–I*) MicroCT images showing sagittal sections of inflamed ankles in 8-wk-old *TNF-tg* and *Shn3^{KA/KA}TNF-tg* mice. Red arrows indicate bone erosion sites (*G*). MicroCT analysis showing trabecular bone mass in the femur. 3D reconstruction images and relative quantification of trabecular bone mass are displayed (*H*). Representative images of calcein/alizarin red labeling and relative histomorphometric quantification of BFR/BS and MAR are displayed (*I*). Yellow arrows indicate the distance between calcein and alizarin labeling (*I*). (*H*, n = 6 ~ 8/group; *I*, n = 7 ~ 10/group). (Scale bars: *G*, 400 μm; *H*, 500 μm; *I*, 50 μm.) (*J*) *Shn3^{+/+}* and *Shn3^{KA/KA}* BMSCs were transfected with the β-catenin-responsive reporter gene (Topflash-Luc) along with *Renilla*, treated with TNF for 24 h, and luciferase activity was measured and normalized to *Renilla* (n = 5). (*K*) mRNA levels of the β-catenin-target gene *Lef1* in tibial RNAs of 8-wk-old *TNF-tg* and *Shn3^{KA/KA}TNF-tg* mice (n = 4). (*L* and *M*) Representative longitudinal sections of femurs from 8-wk-old *TNF-tg* and *Shn3^{KA/KA}TNF-tg*, immunostained for β-catenin (L) or stained for TRAP (*M, Left*). Quantification of TRAP-stained osteoclasts per bone perimeter (*M, Right*). (Scale bars: 50 μm.) (*N*) *Rankl/Opg* mRNA ratio in *Shn3^{+/+}* and *Shn3^{KA/KA}* BMSCs following TNF treatment (n = 4). (*O*) *Shn3^{+/+}* and *Shn3^{KA/KA}* BMSCs were transduced with lentivirus expressing SHN3 proteins (WT, KA, STA), and cultured under osteogenic conditions in the presence of TNF for 6 d. *Rankl/Opg* mRNA ratio was assessed by RT-PCR (n = 4). Values represent mean ± SD: NS, nonsignificant; *$P < 0.05$; **$P < 0.01$; ***$P < 0.001$; ****$P < 0.0001$ by ordinary one-way ANOVA with Dunnett's multiple comparisons test (*E, F, H,* and *O*) or a two-tailed unpaired Student's *t* test for comparing two groups (*I, K,* and *N*).

constructs (29, 43). Additionally, the bone-targeting peptide motif, ((AspSerSer)$_6$, DSS) (44) was grafted onto VP2 capsid protein of AAV9 vector (DSS.rAAV9) to detarget transduction from nonrelevant tissues (29).

We demonstrate that a single IV injection of DSS.rAAV9 carrying *amiR-Shn3* was able to efficiently silence *Shn3* expression in osteoblast-lineage cells residing in the long bones and inflamed ankles of SKG mice and to promote osteoblast-mediated bone formation while reducing osteoclast-mediated bone resorption, resulting in attenuation of articular bone erosions and systemic bone loss. Again of note, AAV-mediated silencing of *Shn3* does not affect immune responses in RA. Thus, bone-targeting AAV-mediated silencing of *Shn3* could be a promising and safe therapeutic strategy to treat bone loss in RA. Future vector modifications could also be made to limit the expression of *amiR-Shn3* in RA settings using inflammation-responsive promoters, which would allow for even more precise expression of therapeutic gene(s) and avoidance of nonskeletal adverse effects.

Although current disease modifying drugs may prevent or slow the formation of new articular erosions, they are unable to repair existing articular and systemic bone damage. Several therapeutic agents to address bone loss act by inhibiting osteoclast-mediated bone resorption are available. However, these are accompanied by many potential untoward side effects, including atypical femoral fractures and osteonecrosis of the jaw. Anabolic agents used in this setting to promote bone formation and repair are limited in number and newly developed agents, such as the anti-SOST antibody (Romosozumab) and the small molecule inhibitor of Cathepsin K (Odanacatib), show off-target cardiovascular and cerebrovascular events in clinical trials, respectively (45, 17). Thus, effective anabolic targets that can limit articular erosion and systemic bone loss are important to pursue.

Materials and Methods

Animals. SKG mice were obtained from Dr. Shimon Sakaguchi (Kyoto University, Japan) and maintained on BALB/c background. Human TNF transgenic (tg) mice were obtained from Dr. George Kollias (Alexander Fleming Biomedical Science Research Center, Greece). *Shn3*$^{-/-}$ (BALB/c), *Shn3*$^{fl/fl}$ (C57BL/6), and *Shn3*$^{KA/KA}$ (C57BL/6) mice were obtained from Dr. Laurie Glimcher (Harvard/DFCI, USA) and Dr. Matthew Greenblatt (Weil Cornell Medicine). *Shn3*$^{-/-}$;SKG mice were generated by crossing *Shn3*$^{-/-}$ mice with SKG mice and maintained on BALB/c background. *Shn3*$^{fl/fl}$ or *Shn3*$^{KA/KA}$ mice were crossed with TNF-tg mice to generate generated *Shn3*$^{fl/fl}$;TNF-tg or *Shn3*$^{KA/KA}$;TNF-tg mice, respectively (C57BL/6). Prrx1-Cre transgenic mice (C57BL/6) were purchased from The Jackson Laboratory, crossed with *Shn3*$^{fl/fl}$ mice, and maintained on the C57BL/6J background. Mouse genotypes were determined by PCR on tail genomic DNA. All animals were used in accordance with the NIH Guide for the Care and Use of Laboratory Animals and were handled according to protocols approved by the University of Massachusetts Chan Medical School committee on animal care (IACUC).

Mouse Models of Inflammatory Arthritis. Ten-week-old female SKG mice were injected intraperitoneally (i.p.) with curdlan (6 mg/kg, dissolved in PBS, Fujifilm Wako Pure Chemical, #032-09902) to accelerate inflammatory arthritis. Clinical peripheral joint inflammation scoring and measurement of ankle thickness using a digital caliper were performed weekly according to an established protocol (46, 47). Histologic inflammation and articular erosions were assessed in paraffin-embedded hind limb tissue sections. H&E-stained sections were scored for inflammation, and H&E and adjacent TRAP-stained sections were used to score articular erosions. Fifty sections were cut from each sample and sections 10, 20, 30, 40, and 50 were scored as previously described (47) by observers blinded to sample identifiers.

Human TNF-tg mice were allowed to develop arthritis until 12 wk of age. Histologic samples from hind limbs were prepared, and scoring was performed as described above.

For K/BxN serum transfer arthritis (STA), KRN T cell transgenic mice (31) were crossed with NOD mice. Arthritogenic serum was obtained from arthritic progeny and 100 μl of the serum was transferred to 5-wk-old male *Shn3*$^{fl/fl}$ and *Shn3*^{Prx1} mice via i.p. injection on days 0, 2, and 7. Clinical peripheral joint inflammation scoring and ankle thickness measurements were performed every other day as previously described (47). Histologic samples from hind limbs were prepared as described above, and scoring of inflammation and articular erosions was performed as previously described (47).

Osteoblast and Osteoclast Culture and Differentiation. Primary calvarial osteoblasts (COBs) were isolated from calvaria of *Shn3*$^{+/+}$ and *Shn3*$^{-/-}$ neonates at postnatal day 3, using collagenase type II (50 mg/mL, Worthington, #LS004176)/dispase II (100 mg/mL, Roche, #10165859001), and cultured in α-MEM medium (Corning) containing 10% FBS (Corning), 2 mM L-glutamine (Corning), 1% penicillin/ streptomycin (Corning) and 1% nonessential amino acids (Corning). Alternatively, mouse bone marrow-derived mesenchymal stromal cells (BMSCs) were isolated from crushed long bones of 8-wk-old mice and cultured in α-MEM medium with 10% FBS. Human BMSCs were purchased from ScienCell Research Laboratories and cultured according to the manufacturer's manual. For osteogenic differentiation, cells were maintained in α-MEM containing 10% FBS, 2 mM L-glutamine, 1% penicillin/ streptomycin and 1% nonessential amino acids, and differentiated with ascorbic acid (200 μM, Sigma, #A8960) and β-glycerophosphate (10 mM, Sigma, #G9422). Ocy454 cells were maintained in α-MEM medium supplemented with 10% FBS at 33 °C with 5% CO$_2$. For osteocyte differentiation, cells were grown at 33 °C and were allowed to become confluent. They were then transferred to 37 °C and cultured for 6 d (48). Cells were then stimulated with TNF (20 ng/mL), IL-17A (50 ng/mL) or TNF plus IL-17A for 6 h. For alkaline phosphatase (ALP) activity, cells were subsequently washed with phosphate-buffered saline (PBS) and incubated with a solution containing 6.5 mM Na$_2$CO$_3$, 18.5 mM NaHCO$_3$, 2 mM MgCl$_2$, and phosphatase substrate (Sigma, S0942), and ALP activity was measured by spectrometer (Biorad). To detect extracellular matrix mineralization in mature osteoblasts, cells were washed with PBS and fixed in 70% EtOH for 15 min at room temperature. Mineralization was quantified by the acetic acid extraction method and measured using a spectrometer.

For preparation of bone marrow monocytes (BMMs), femurs were dissected from 8-wk-old mice (C57BL/6J), and cells were collected by flushing and plated overnight in α–MEM with 10% FBS. Nonadherent cells were collected and cultured in the presence of M-CSF (20 ng/mL, R&D systems, #416-ML-010) for 24 h to obtain monocytes. Alternatively, cells were differentiated into osteoclasts in the presence of M-CSF (20 ng/mL) and RANKL (10 ng/mL, R&D systems, #462-TEC-010). Cells were then stimulated with TNF (20 ng/mL), IL-17A (50 ng/mL) or TNF plus IL-17A for 6 h. For the TRAP activity assay, the supernatant from osteoclast cultures was incubated with a mixture of 0.1 M acetate solution (Sigma, #3863), 90 mM C$_4$H$_4$Na$_2$O$_6$, and 7.6 mM p-nitrophenyl phosphate at 37 °C for 1 h, added with 3N NaOH, and measured by spectrometer. Alternatively, cells were plated into Osteo Assay surface plates (Corning Life Sciences, #3987), and osteoclast resorption activity was measured according to the manufacturer's instructions.

Isolation of Synovial Cells. Synovium was dissected from ankles of mice, cut into small pieces, and digested for 30 min with DNase I 0.1 mg/mL (Roche) and Collagenase type IV 1 mg/mL (Worthington) in RPMI at 37 °C. The tissue was then mechanically dissociated over a 70-μm cell strainer and a cell suspension was prepared. Isolated cells were amplified in DMEM supplemented with 10% FBS and 1% penicillin–streptomycin (49, 50).

Construction of Shn3 Plasmids. To generate Flag-tagged SHN3 constructs, murine *Shn3* cDNA was PCR amplified and cloned into the pHASE/PGK-PURO lentiviral vector. Constructs were as follows: (all aa numbering relative to the reference sequence NP_001121186.1): SHN3-WT (p.1-1,084 aa), SHN3-ΔD (Δ902-910 aa of p.1-1,084 aa), SHN3-KA (K886/K887/K888 substituted to alanine, p.1-1,084 aa), and SHN3-STA (S810/S811/T851/S911/S913 substituted to alanine, p.1-1,084 aa). His-SHN3-WT (p.50-936 aa), His-SHN3-KA (K886/K887/K888 substituted to alanine, p.50-936 aa), His-SHN3-STA (S810/S811/T851/S911/S913 substituted to alanine. p.50-936 aa) were PCR amplified and cloned into pFastBac (Invitrogen) vector. The shRNA targeting human *SHN3* was cloned

into pLKO.1-TRC lentiviral vector. The shRNA sequences are listed in *SI Appendix*, Table S1.

Antibodies and Reagents. Antibodies specific to P-Ser/Thr (#9631), P-ERK1/2 (#4376), P-p38 (#9211), P-JNK1/2 (#4668), and FLAG (#14793) were purchased from Cell Signaling Technology. Anti-human SHN3 antibody (#PA5-52194) and recombinant TNF (#210-TA) and IL-17A (#7955-IL) were purchased from ThermoFisher Scientific and R&D Systems, respectively. The inhibitors specific to ERK (U0126, #1144), p38 (SB203580, #1202), and JNK (SP600125, #1496) were purchased from Tocris Bioscience.

rAAV Design and Treatment. Bone-targeting rAAV9s carrying *amiR-Ctrl* or *amiR-Shn3* were designed and generated as previously reported (29). A single dose of 4×10^{11} genome copies of rAAV9 carrying *amiR-Ctrl* or *amiR-Shn3* was intravenously (i.v.) injected to 8-wk-old female SKG mice.

Flow Cytometry Analysis for Immune Cells. Multicolor flow cytometric analysis was carried out using an LSR II with DIVA software (BD Biosciences). Analysis was conducted with FlowJo software (TreeStar, Ashland, OR). Splenocytes were harvested from 8-wk-old mouse spleens and B and T cells were isolated using CD45/B220-conjugated or CD4-conjugated IMag antimouse magnetic particles, (BD Biosciences, #551513 and #551539, respectively). Splenic and synovial myeloid and lymphoid cells were identified using the following fluorochrome-labeled antibodies: BV510-conjugated CD11b (M1/70, Biolegend, #101263), FITC-conjugated LY6C (HKL4, Biolegend, #128006), PE-Cy7-conjugated LY6G (1A8, Biolegend, #127617), PE-Cy7-conjugated B220 (RA3-6B2, Tonbo Biosciences, #60-0452-4100), APC-conjugated CD3e (145-2C11, BD Pharmingen, #553066), PerCP-Cy5.5- conjugated CD4 (GK1.5, Tonbo Biosciences, #65-0041-4025), FITC-conjugated CD8 (53-6.7, Tonbo Biosciences, #35-0081-4025). Cell suspensions were incubated in Fc block 2.4G2 supernatant (2.4G2 hybridoma; ATCC) before staining. Cells were stimulated with TNF (20 ng/mL), IL-17A (50 ng/mL) or TNF plus IL-17A for 6 h.

MicroCT Analysis. MicroCT 35 scanner (Scanco Medical) was used for qualitative and quantitative assessment of trabecular and cortical bone microarchitecture and performed by an investigator blinded to the genotypes of the animals under analysis. Femurs and ankles excised from the indicated mice were measured using a microCT 35 scanner with a spatial resolution of 7 μm and 12 μm, respectively. For trabecular bone analysis of the distal femur, an upper 2.1 mm region beginning 280 μm proximal to the growth plate was contoured. MicroCT scans of inflamed ankles were performed using isotropic voxel sizes of 12 μm. For cortical bone analysis of femur and tibia, a midshaft region of 0.6 mm in length was used. 3D reconstruction images were obtained from contoured 2D images by methods based on distance transformation of the binarized images. Alternatively, the Inveon multimodality 3D visualization program was used to generate fused 3D viewing of multiple static or dynamic volumes of microCT modalities (Siemens Medical Solutions USA, Inc). All images presented are representative of the respective genotypes (n > 5).

Histology, Histomorphometry, Immunohistochemistry, and Immunofluorescence Staining.
Histology. Femurs or ankles were dissected from the mice, fixed in 10% neutral buffered formalin for 2 d, and decalcified by daily changes of 15% tetrasodium EDTA for 3 to 4 wk. Tissues were dehydrated by passage through an ethanol series, cleared twice in xylene, embedded in paraffin, and sectioned at 6 μm thickness along the coronal plate from anterior to posterior. Decalcified femur and ankle sections were stained with hematoxylin and eosin (H&E) or tartrate-resistant acid phosphatase (TRAP) as previously described (29).
Histomorphometric analysis. Calcein (25 mg/kg; Sigma, #C0875) and alizarin-3-methyliminodiacetic acid (50 mg/kg; Sigma, #A3882) dissolved in 2% sodium bicarbonate solution were subcutaneously injected into mice at a 5-d interval. After a 2-d fixation in 10% neutral buffered formalin, undecalcified femur samples were embedded in methylmethacrylate. Proximal metaphyses were sectioned longitudinally (5 μm), and a region of interest was defined. Bone formation rate/bone surface (BFR/BS), mineral apposition rate (MAR), bone area (B.Ar), and osteoclast number/bone perimeter (N.Oc/B.Pm) were measured using a Nikon Optiphot 2 microscope interfaced to a semiautomatic analysis system (Osteometrics). Measurements were taken on two sections/

sample (separated by ~25μm) in a blinded fashion and summed prior to normalization to obtain a single measure/sample in accordance with ASBMR standards (51). This methodology has undergone extensive quality control and validation.
Immunohistochemistry. Paraffin sections were dewaxed and stained using the Discovery XT automated immunohistochemistry stainer (Ventana Medical Systems, Inc.). CC1 standard (pH 8.4 buffer contained Tris/Borate/EDTA) and inhibitor D (3% H_2O_2, endogenous peroxidase) were used for antigen retrieval and blocking, respectively. Sections were incubated with antibodies specific to osteocalcin (1:100, LSBio, # LS-C17044) or β-catenin (1:100, Cell signaling, #8480) overnight at 4 °C and a secondary antibody of VisUCyte™ HRP Polymer (R&D systems, #VC005) for 30 min at room temperature. Substrate working solution (DAB substrate kit, Vector Sk-4100) was added to the sections at room temperature for 1 to 2 min followed by hematoxylin and bluing reagent counterstain at 37 °C.
Immunofluorescence. Femur and ankle bones were fixed with 4% paraformaldehyde (PFA) for 2 d and decalcified in 0.5 M tetrasodium EDTA solution for 10 d. Semidecalcified samples were infiltrated with 25% sucrose phosphate for 4 d. All samples were embedded in 50/50 mixture of 25% sucrose solution and optimal cutting temperature (OCT) compound (Sakura) and cut into 12-μm-thick sagittal sections using a cryostat (Leica). Cryosectioned femur or ankle samples from 8-wk-old mice were stained with antibodies for cathepsin K (1:150, ABclonal, #A1782), osteocalcin (1:100, ABclonal, #A6205), or CD248 (1:100, Abnova, #PAB13304). Alexa Fluor 594 (1:400, Thermo, A11032) was used as a secondary antibody.

Measurement of Serum Ctx-1 and Osteocalcin. The ELISA kits for Ctx-1 (MC0850) or osteocalcin (RK03088) were purchased from ABclonal technology and used to measure serum levels of Ctx-1 or osteocalcin after overnight fasting.

Luciferase Assay. β-catenin-responsive reporter gene (TopFlash-luc) and *Renilla* luciferase vector (Promega) were transfected into BMSCs using the Effectene transfection reagent (Qiagen). After 48 h, dual luciferase assays were performed according to the manufacturer's protocol (Promega), and TopFlash luciferase activity was normalized to *Renilla*.

In Vitro Kinase Assay. A total of 200 ng of recombinant ERK2 (New England Biolabs, #P6080) and 300 ng of purified His-SHN3 proteins (p.50-936 aa or p.630-936 aa: WT, KA, STA) were incubated in kinase buffer (20 mM HEPES, pH 7.5, 20 mM MgCl$_2$, 1 mM EDTA, 2 mM NaF, 2 mM-glycerophosphate, 1 mM DTT, 10 μM ATP) containing 10 μCi of γ32P-ATP (PerkinElmer) for 15 min at 30 °C. The phosphorylated proteins were visualized by autoradiography.

RT-PCR, Immunoprecipitation, and Immunoblotting. Tibial bones were chopped and homogenized using the Beadbug microtube homogenizer, total RNA was extracted using QIAzol (QIAGEN), and cDNA was synthesized using the High-Capacity cDNA Reverse Transcription Kit from Applied Biosystems. Quantitative RT-PCR was performed using SYBR® Green PCR Master Mix (Bio-Rad, Hercules, CA) with the Bio-Rad CFX Connect Real-Time PCR detection system. Ribosomal protein, large, P0 (Rplp0) was used as a housekeeping gene. The primers used for PCR are listed in *SI Appendix*, Table S2.

Primary COBs expressing Flag-Shn3 proteins were lysed with lysis buffer [50 mM Tris-HCl (pH 7.4), 150 mM NaCl, 1% Triton X-100, 1 mM EDTA, 1 mM EGTA, 50 mM NaF, 1 mM Na$_3$VO$_4$, 1 mM PMSF and protease inhibitor cocktail (Sigma)]. Proteins from cell lysates were immunoprecipitated with Flag-conjugated agarose (Sigma, A2220) and subjected to SDS-PAGE, transferred to Immobilon-P membranes (Millipore), immunoblotted with the indicated antibodies, and developed with ECL (Thermoscientific). Immunoblotting using antibodies specific to FLAG served as a loading control.

Human Tissues and Analyses. Five deidentified synovial/bone samples were obtained from metatarsal head resection arthroplasty surgeries on RA patients from Yonsei University Severance Hospital, Korea. Synovium and/or bone in these samples were examined by H&E staining and immunostained for SHN3. These were obtained under Institutional Review Board approval (IRB No.4-2019-0506) for histology and immunohistochemistry.

Statistical Analysis and Reproducibility. All experiments were repeated two or three times, for immunofluorescence, immunohistochemistry, histology,

immunoblotting, and RT-PCR. All data are shown as the mean ± SD. We first performed the Shapiro–Wilk normality test for checking normal distribution of the groups. If the normality test was passed, a two-tailed, unpaired Student's t test was used. If the normality test failed, the Mann–Whitney test was used for the comparisons between two groups. For the comparisons of three groups, we used a one-way ANOVA if the normality test was passed, followed by Tukey's multiple comparison test for all groups. GraphPad PRISM software (ver.9.0.2, La Jolla, CA) was used for statistical analysis.

Data, Materials, and Software Availability. All study data are included in the article and/or *SI Appendix*.

Author affiliations: ^{a}Department of Medicine, Division of Rheumatology, University of Massachusetts Chan Medical School, Worcester, MA 01605; ^{b}Horae Gene Therapy Center, University of Massachusetts Chan Medical School, Worcester, MA 01605; ^{c}Li Weibo Institute for Rare Diseases Research, University of Massachusetts Chan Medical School, Worcester, MA 01605; ^{d}Endocrine Unit, Massachusetts General Hospital, Harvard Medical School, Boston, MA 02114; ^{e}Department of Orthopaedic Surgery, Yonsei University College of Medicine, Seoul 03722, South Korea; ^{f}Department of Microbiology and Physiological Systems, University of Massachusetts Chan Medical School, Worcester, MA 01605; ^{g}Viral Vector Core, University of Massachusetts Chan Medical School, Worcester, MA 01605; and ^{h}Department of Medicine, Division of Rheumatology, Inflammation and Immunity, Brigham and Women's Hospital, Harvard Medical School, Boston, MA 02115

Author contributions: Z.S., J.-M.K., E.M.G., and J.-H.S. designed research; Z.S., J.-M.K., Y.-S.Y., K.N., S.C., and T.S. performed research; K.H.P. and G.G. contributed new reagents/analytic tools; Z.S., J.-M.K., E.M.G., and J.-H.S. analyzed data; and Z.S., J.-M.K., E.M.G., and J.-H.S. wrote the paper.

1. E. M. Gravallese *et al.*, Synovial tissue in rheumatoid arthritis is a source of osteoclast differentiation factor. *Arthritis Rheumatol.* **43**, 250–258 (2000).
2. W. O'Brien *et al.*, RANK-independent osteoclast formation and bone erosion in inflammatory arthritis. *Arthritis Rheumatol.* **68**, 2889–2900 (2016).
3. N. C. Walsh *et al.*, Osteoblast function is compromised at sites of focal bone erosion in inflammatory arthritis. *J. Bone Miner. Res.* **24**, 1572–1585 (2009).
4. D. Diarra *et al.*, Dickkopf-1 is a master regulator of joint remodeling. *Nat. Med.* **13**, 156–163 (2007).
5. C. Wehmeyer *et al.*, Sclerostin inhibition promotes TNF-dependent inflammatory joint destruction. *Sci. Transl. Med.* **8**, 330ra335 (2016).
6. U. Harre *et al.*, Glycosylation of immunoglobulin G determines osteoclast differentiation and bone loss. *Nat. Commun.* **6**, 6651 (2015).
7. I. B. McInnes, G. Schett, The pathogenesis of rheumatoid arthritis. *N. Engl. J. Med.* **365**, 2205–2219 (2011).
8. J. Widdifield *et al.*, Access to rheumatologists among patients with newly diagnosed rheumatoid arthritis in a Canadian universal public healthcare system. *BMJ Open* **4**, e003888 (2014).
9. G. Schett, E. Gravallese, Bone erosion in rheumatoid arthritis: mechanisms, diagnosis and treatment. *Nat. Rev. Rheumatol.* **8**, 656–664 (2012).
10. T. Dimitroulas, S. N. Nikas, P. Trontzas, G. D. Kitas, Biologic therapies and systemic bone loss in rheumatoid arthritis. *Autoimmun. Rev.* **12**, 958–966 (2013).
11. N. C. Wright *et al.*, Arthritis increases the risk for fractures–results from the Women's Health Initiative. *J. Rheumatol.* **38**, 1680–1688 (2011).
12. G. Haugeberg, J. A. Falch, J. I. Halse, T. K. Kvien, Bone mineral density and frequency of osteoporosis in female patients with rheumatoid arthritis: Results from 394 patients in the Oslo County Rheumatoid Arthritis register. *Arthritis Rheumatism* **43**, 522–530 (2000).
13. F. Borumandi, T. Aghaloo, L. Cascarini, A. Gaggl, K. Fasanmade, Anti-resorptive drugs and their impact on maxillofacial bone among cancer patients. *Anticancer Agents Med. Chem.* **15**, 736–743 (2015).
14. P. Esbrit, M. J. Alcaraz, Current perspectives on parathyroid hormone (PTH) and PTH-related protein (PTHrP) as bone anabolic therapies. *Biochem. Pharmacol.* **85**, 1417–1423 (2013).
15. M. Augustine, M. J. Horwitz, Parathyroid hormone and parathyroid hormone-related protein analogs as therapies for osteoporosis. *Curr. Osteoporos Rep.* **11**, 400–406 (2013).
16. M. E. Kraenzlin, C. Meier, Parathyroid hormone analogues in the treatment of osteoporosis. *Nat. Rev. Endocrinol.* **7**, 647–656 (2011).
17. K. G. Saag *et al.*, Romosozumab or alendronate for fracture prevention in women with osteoporosis. *N. Engl. J. Med.* **377**, 1417–1427 (2017).
18. J. H. Shim *et al.*, Schnurri-3 regulates ERK downstream of WNT signaling in osteoblasts. *J. Clin. Invest.* **123**, 4010–4022 (2013).
19. D. C. Jones *et al.*, Regulation of adult bone mass by the zinc finger adapter protein Schnurri-3. *Science* **312**, 1223–1227 (2006).
20. M. N. Wein *et al.*, Control of bone resorption in mice by Schnurri-3. *Proc. Natl. Acad. Sci. U.S.A.* **109**, 8173–8178 (2012).
21. R. Xu *et al.*, Targeting skeletal endothelium to ameliorate bone loss. *Nat. Med.* **24**, 823–833 (2018).
22. M. M. Matzelle *et al.*, Resolution of inflammation induces osteoblast function and regulates the Wnt signaling pathway. *Arthritis Rheum.* **64**, 1540–1550 (2012).
23. N. Sakaguchi *et al.*, Altered thymic T-cell selection due to a mutation of the ZAP-70 gene causes autoimmune arthritis in mice. *Nature* **426**, 454–460 (2003).
24. J. Keffer *et al.*, Transgenic mice expressing human tumour necrosis factor: a predictive genetic model of arthritis. *EMBO J.* **10**, 4025–4031 (1991).
25. B. Osta, F. Lavocat, A. Eljaafari, P. Miossec, Effects of Interleukin-17A on Osteogenic Differentiation of Isolated Human Mesenchymal Stem Cells. *Front Immunol.* **5**, 425 (2014).
26. F. Lavocat, B. Osta, P. Miossec, Increased sensitivity of rheumatoid synoviocytes to Schnurri-3 expression in TNF-alpha and IL-17A induced osteoblastic differentiation. *Bone* **87**, 89–96 (2016).
27. H. Yoshitomi *et al.*, A role for fungal {beta}-glucans and their receptor Dectin-1 in the induction of autoimmune arthritis in genetically susceptible mice. *J. Exp. Med.* **201**, 949–960 (2005).
28. H. Hata *et al.*, Distinct contribution of IL-6, TNF-alpha, IL-1, and IL-10 to T cell-mediated spontaneous autoimmune arthritis in mice. *J. Clin. Invest.* **114**, 582–588 (2004).
29. Y. S. Yang *et al.*, Bone-targeting AAV-mediated silencing of Schnurri-3 prevents bone loss in osteoporosis. *Nat. Commun.* **10**, 2958 (2019).
30. A. D. Christensen, C. Haase, A. D. Cook, J. A. Hamilton, K/BxN Serum-transfer arthritis as a model for human inflammatory arthritis. *Front Immunol.* **7**, 213 (2016).
31. A. S. Korganow *et al.*, From systemic T cell self-reactivity to organ-specific autoimmune disease via immunoglobulins. *Immunity* **10**, 451–461 (1999).
32. M. Logan *et al.*, Expression of Cre recombinase in the developing mouse limb bud driven by a Prxl enhancer. *Genesis* **33**, 77–80 (2002).
33. G. Sabio, R. J. Davis, TNF and MAP kinase signalling pathways. *Semin. Immunol.* **26**, 237–245 (2014).
34. T. Liu, L. Zhang, D. Joo, S. C. Sun, NF-kappaB signaling in inflammation. *Signal. Transduct. Target. Ther.* **2**, 17023- (2017).
35. B. Osta, G. Benedetti, P. Miossec, Classical and paradoxical effects of TNF-alpha on bone homeostasis. *Front. Immunol.* **5**, 48 (2014).
36. M. Oukka *et al.*, A mammalian homolog of Drosophila schnurri, KRC, regulates TNF receptor-driven responses and interacts with TRAF2. *Mol. Cell* **9**, 121–131 (2002).
37. M. Oukka, M. N. Wein, L. H. Glimcher, Schnurri-3 (KRC) interacts with c-Jun to regulate the IL-2 gene in T cells. *J. Exp. Med.* **199**, 15–24 (2004).
38. R. Baron, M. Kneissel, WNT signaling in bone homeostasis and disease: From human mutations to treatments. *Nat. Med.* **19**, 179–192 (2013).
39. C. P. Venditti, Safety questions for AAV gene therapy. *Nat. Biotechnol.* **39**, 24–26 (2021).
40. L. Vandenberghe, J. Wilson, G. Gao, Tailoring the AAV vector capsid for gene therapy. *Gene Therapy* **16**, 311–319 (2009).
41. D. Grimm *et al.*, Fatality in mice due to oversaturation of cellular microRNA/short hairpin RNA pathways. *Nature* **441**, 537–541 (2006).
42. J. L. McBride *et al.*, Artificial miRNAs mitigate shRNA-mediated toxicity in the brain: implications for the therapeutic development of RNAi. *Proc. Natl. Acad. Sci. U.S.A.* **105**, 5868–5873 (2008).
43. J. Xie *et al.*, Effective and accurate gene silencing by a recombinant AAV-Compatible microRNA scaffold. *Mol Ther.* **28**, 422–430 (2020).
44. G. Zhang *et al.*, A delivery system targeting bone formation surfaces to facilitate RNAi-based anabolic therapy. *Nat. Med.* **18**, 307–314 (2012).
45. A. Mullard, Merck & Co. drops osteoporosis drug odanacatib. *Nat. Rev. Drug Discov.* **15**, 669 (2016).
46. K. K. Keller *et al.*, SKG arthritis as a model for evaluating therapies in rheumatoid arthritis with special focus on bone changes. *Rheumatol. Int.* **33**, 1127–1133 (2013).
47. A. R. Pettit *et al.*, TRANCE/RANKL knockout mice are protected from bone erosion in a serum transfer model of arthritis. *Am. J. Pathol.* **159**, 1689–1699 (2001).
48. J. M. Spatz *et al.*, The Wnt inhibitor sclerostin is up-regulated by mechanical unloading in osteocytes in Vitro. *J. Biol. Chem.* **290**, 16744–16758 (2015).
49. M. H. Chang *et al.*, Arthritis flares mediated by tissue-resident memory T cells in the joint. *Cell. Rep.* **37**, 109902 (2021).
50. J. Zhao *et al.*, A protocol for the culture and isolation of murine synovial fibroblasts. *Biomed Rep.* **5**, 171–175 (2016).
51. D. W. Dempster *et al.*, Standardized nomenclature, symbols, and units for bone histomorphometry: a 2012 update of the report of the ASBMR Histomorphometry Nomenclature Committee. *J. Bone Miner. Res.* **28**, 2–17 (2013).